Analysis of circular gratings as image plane coronagraph filters

François Hénault

Version of Record: https://www.sciencedirect.com/science/article/pii/S0030401822003017
Manuscript_f08a79d15b3241ce8fadb1597be83ff0

Analysis of circular gratings as image plane coronagraph filters

François Hénault
Institut de Planétologie et d'Astrophysique de Grenoble
Université Grenoble-Alpes, Centre National de la Recherche Scientifique
B.P. 53, 38041 Grenoble – France

ABSTRACT

Coronagraphy is an efficient technique for identifying and characterizing extra-solar planets orbiting in the habitable zone of their parent star. An important family of coronagraphs is based on amplitude or phase filters placed at an intermediate image plane of the optical system, spreading starlight outside of the so-called "Lyot stop" located at the exit pupil plane of the instrument. This article explores the potential of circular amplitude and phase gratings employed as image plane coronagraph filters. It presents a theoretical analysis of the simplest case of an amplitude circular grating and introduces an inversion paradigm with respect to classical Lyot coronagraph, by exchanging its image and pupil masks. Various types of circular gratings are considered and their performance is evaluated with the help of numerical simulations. The most promising solutions are presented and discussed. The main conclusion is that high attenuation ratios of the parent star are feasible, provided that the system is properly optimized with a Lyot stop especially tailored to the grating filter.

Keywords: Coronagraphy, Circular grating, Fourier optics

1 INTRODUCTION

In the forthcoming years, coronagraphy will probably be the most efficient technique for identifying and characterizing extra-solar planets orbiting in the habitable zone of their parent star, as already demonstrated by the ground instruments SPHERE [1] and GPI [2] in operation on the Very Large Telescope (VLT) and Gemini South telescope respectively. Future space observatories like WFIRST-AFTA [3] also are in construction. The present paper is especially focused on Lyot type coronagraphs (LTC), where an amplitude or phase filter is located at an intermediate image plane of the optical system, and diffracts starlight outside of the diameter of a "Lyot stop" placed at the exit pupil of the instrument, before finally focusing the beam at the image plane of the instrument. Among this family, one will find the historical Lyot coronagraph where the image filtering is achieved with a small-size central blocking mask [4]. Later came the circular and phase knife coronagraph (PMC), making use of nulling phase jumps at the focal plane of the telescope [5-6]. More recently, the concept of optical vortex coronagraph [7-8] exhibits higher potential performance in terms of null depth and throughput, or planet transmission factor. Extensive reviews of these different types of coronagraphs and of their achievable performance can be found in Refs [9-10]. But so far, little attention was paid to circular amplitude or phase gratings applied to coronagraphy [11]. From pioneering theoretical studies [12-14], it seems that they were essentially considered for laser beam shaping [15], metrology [16] or particles trapping applications [17-18]. The scope of this paper is to explore the vast realm of circular gratings employed as image plane coronagraph filters, either of the amplitude or phase types. In the latter case, this can be achieved by means of transmitting phase plates as sketched in Figure 1.

The paper is divided into the following sections:

- Firstly, section 2presents a theoretical analysis of the simple case of an amplitude circular grating set at the image plane of a coronagraph, and the resulting intensity distribution formed in the Lyot stop plane. It then introduces a necessary condition for achieving deep extinction. It entails an inversion paradigm with respect to a classical LTC that consists in setting the central blocking mask in a pupil plane instead of the image plane.

- Section 3 describes the various types of Circular amplitude gratings (CAG) and Circular phase gratings (CPG), the employed numerical models and a first set of circular gratings designs.

- From these most promising solutions, numerical simulations are carried out in order to evaluate the achievable performance in terms of star nulling ratio and planet transmission in section 4.

- Finally, section 5 summarizes the main lessons drawn from the study.

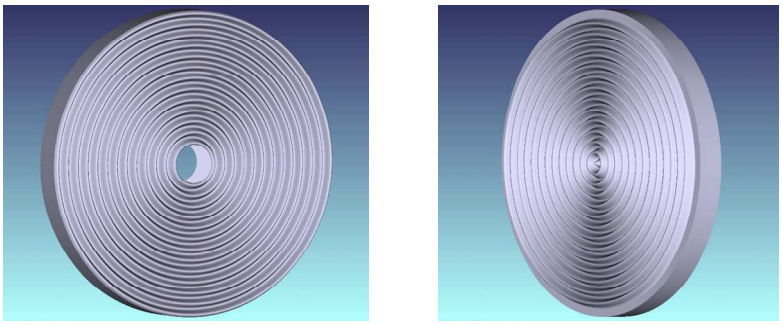

Figure 1: Schematic views of a transmitting circular phase grating (the central hole on the left panel is mainly for illustration purpose).

2 THEORETICAL ANALYSIS

Let us consider the case of a coronagraphic telescope of focal length F and diameter $D = 2R$, equipped with a circular grating in its image plane. The main employed coordinate systems and scientific notations are defined in subsection 2.1. The following subsection (§ 2.2) gives an analytical development for the intensity distribution formed in the Lyot stop plane fir a simple case. The final subsection 2.3 exposes the "inversion paradigm" that results in defining unconventional Lyot stops with central obscuration.

2.1 Mathematical notations and coordinate frames

The general principle of a LTC is illustrated in Figure 2-A. It is usually composed of the following elements, to which four coordinate frames are attached:

- The entrance plane of the coronagraph is located at the exit pupil of the astronomical telescope. Its reference frame is defined as (OXYZ), where O is the pupil centre and OZ the optical axis of the system. Any point P in the OXY plane is defined by Cartesian coordinates (x,y) or polar coordinates (ρ,θ').

- The diffractive element is located in the image plane of the telescope. It can either be a central blocking mask as in Bernard Lyot's historical concept [4], or a phase mask in modern Phase mask coronagraphs (PMC) designs [5-8]. The attached coordinate system is (O'X'Y'Z), with O' the centre of the diffractive mask located along the optical axis OZ. Any point M' in the O'X'Y' plane is defined by its Cartesian coordinates (x',y') or polar coordinates (ρ',θ'). They can also be expressed in terms of λ/D, with λ the wavelength and D the telescope diameter.

- The Lyot stop is optically conjugated with the pupil plane OXY. The attached coordinate system is (O"X"Y"Z), with O" the centre of the Lyot stop and $(x",y")$ the Cartesian coordinates of any point P" in the O"X"Y" plane, also denoted $(\rho",\theta")$ in polar coordinates.

- The coronagraph image plane is the final detection plane. The attached coordinate system is (O"'X"'Y"'Z), with O"' the centre of the detector and $(\rho"',\theta"')$ the polar coordinates of any point M"' at the detector surface. They can also be expressed in terms of λ/D, with λ the wavelength and D the telescope diameter.

All employed coordinate systems are illustrated in Figure 3. The diameters of the telescope exit pupil and of the Lyot stop are noted $D = 2R$ and $D_L = 2R_L$ respectively For the sake of simplicity, we assume identical focal length F for the

telescope and all focusing and collimating optics downstream. It implies a magnification factor equal to unity between the input pupil and Lyot stop planes. It must be noted that all optics sketched as lenses in Figure 3 could be preferably mirrors in reality. Moreover, the theoretical frame of this study is restricted to first-order Gaussian optics and Fraunhofer scalar diffraction. All optics are assumed to be aberration-free. In that case we shall make use of the following mathematical symbols and functions:

λ	The wavelength of light assumed to be monochromatic
$B_D(x,y)$ or $B_D(\rho)$	"Pillbox" function of diameter D, equal to unity when $\rho = \sqrt{x^2+y^2} \leq R = D/2$ inside the telescope pupil, and to zero elsewhere
$A'(x',y')$ or $A'(\rho',\theta')$	Complex amplitude diffracted by the non aberrant telescope pupil into the image plane O'X'Y'
$\hat{B}_D(\rho')$	Fourier transform of $B_D(x,y)$ equal to $2J_1(z)/z$ with $z = \pi D\rho'/\lambda F$, with $J_1(z)$ the type-J Bessel function at the first order
$B'(u',\theta')$ or $B'(r',\theta')$, $B'(r')$]	Amplitude function of the image filter in plane O'X'Y'
$\phi'(u',\theta')$ or $\phi'(r',\theta')$, $\phi'(r')$	Phase function of the image filter in plane O'X'Y'
$A''(\rho'',\theta'')$ or $A''(r'',\theta'')$, $A''(r'')$	Complex amplitude diffracted by the image filter into the Lyot stop plane O"X"Y"
$I''(\rho'',\theta'')$	Intensity distribution at the Lyot stop plane
$A'''(\rho''',\theta''')$	Complex amplitude in the final image plane of the coronagraph O"'X"'Y "'
$N'''(\rho''',\theta''')$	"Nulled" intensity distribution at the coronagraph image plane
p'	Spatial period of the filter in the O'X'Y' plane
$f' = 1 / p'$	Spatial frequency of the filter
i	The complex square root of -1

Finally, it will be assumed that the wavelength λ, the telescope diameter D, and the telescope focal length F are equal to 0.5 µm, 10 m and 200 m respectively, for all the calculations and numerical simulations presented in the following sections 2, 3 and 4. Thus the telescope aperture number N is equal to $N = F / D = 20$. There is no central obscuration in the telescope pupil, excepted when stated explicitly.

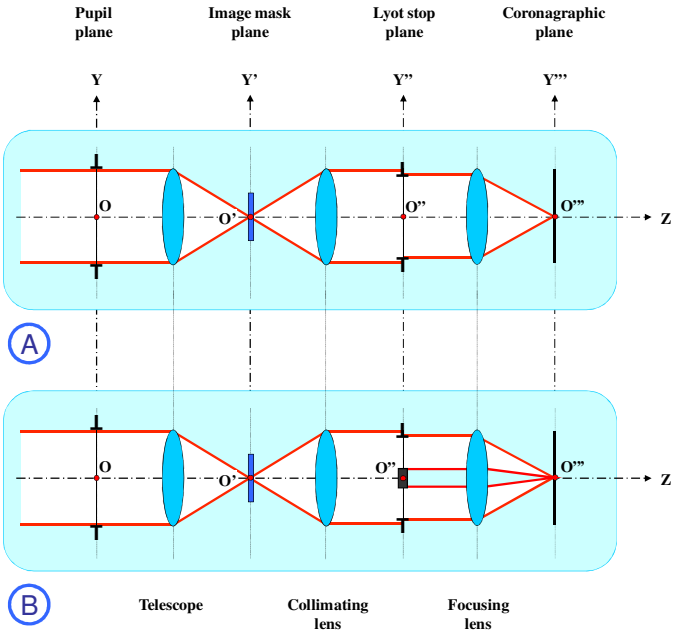

Figure 2: General sketch of a LTC (1) and of the modified layout for circular grating filters (2).

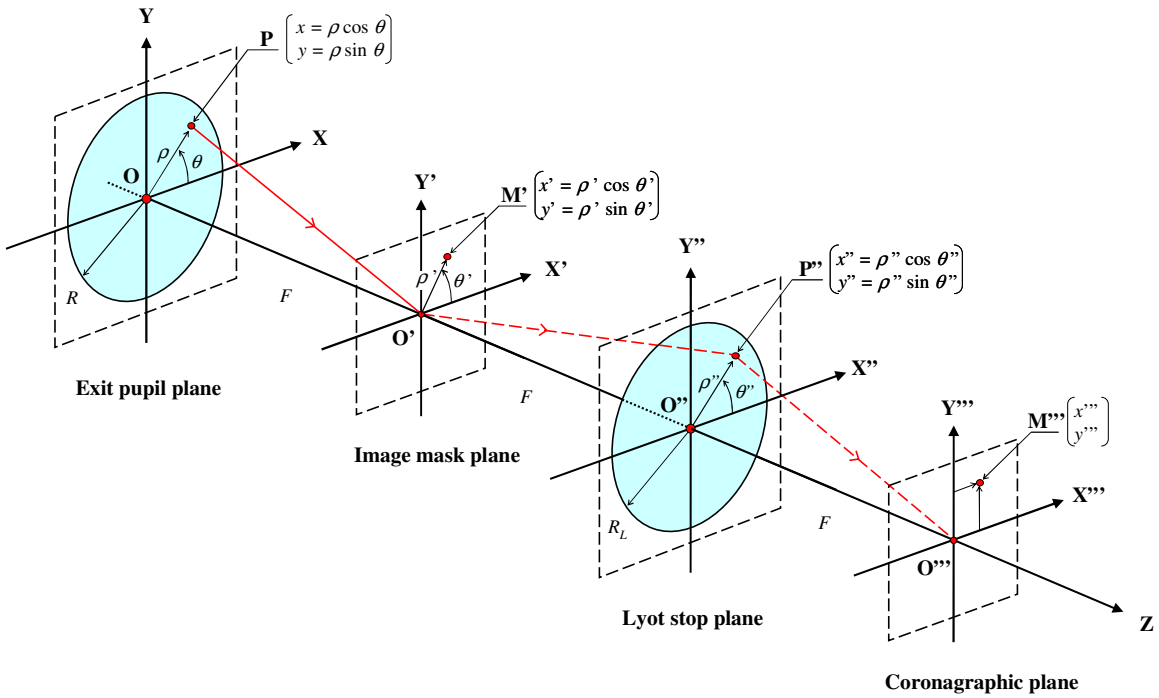

Figure 3: Coordinate systems and scientific notations.

2.2 Analytical expression of Lyot stop intensity

In the frame of first-order Gaussian optics and Fraunhofer scalar diffraction, the diffracted complex amplitude at any point M' (x', y') located in the image plane O'X'Y' is proportional to the Fourier transform of the pupil transmission function $B_D(x, y)$, which writes in Cartesian coordinates:

$$A'(x', y') = K \int_{-\infty}^{+\infty} \int_{-\infty}^{+\infty} B_D(x, y) \exp\left[-2i\pi(xx' + yy')/\lambda F\right] dxdy \,, \tag{1}$$

where K is a normalization factor. From now on will only be used polar instead of Cartesian coordinates. Then Eq. 1 rewrites as [19]:

$$A'(\rho', \theta') = K \int_{0}^{2\pi} \int_{0}^{+\infty} B_D(\rho) \exp\left[-2i\pi\rho\rho' \cos(\theta' - \theta)/\lambda F\right] \rho d\rho d\theta \,. \tag{2}$$

For a circular pupil free of wavefront errors the diffracted complex amplitude is axis symmetric and does not depend on θ'. Eq. 2 is rewritten as:

$$A'(\rho') = K \int_{0}^{+\infty} \int_{0}^{2\pi} B_D(\rho) \exp\left[-2i\pi\rho\rho' \cos\theta/\lambda F\right] d\theta \rho d\rho = \pi R^2 \hat{B}_D(\rho') \,. \tag{3}$$

Inside the coronagraph, the complex amplitude $A''(\rho'',\theta'')$ formed at the Lyot stop plane O"X"Y" is obtained by multiplying $A'(\rho')$ with the complex transmission of the image filter, then taking the inverse Fourier transform of the result. Denoting $B'(\rho',\theta')$ and $\phi'(\rho',\theta')$ the amplitude and phase functions of the filter respectively, it yields:

$$A''(\rho'',\theta'') = K' \int_0^{2\pi} \int_0^{+\infty} A'(\rho') B'(\rho',\theta') \exp[i\phi'(\rho',\theta')] \exp[2i\pi\rho'\rho'' \cos(\theta''-\theta')/\lambda F] \rho' d\rho' d\theta', \tag{4}$$

where *K*' is the normalization factor. Since our study is limited to the case of radial amplitude and phase functions, $B'(\rho',\theta')$ and $\phi'(\rho',\theta')$ only depend on the radial coordinate ρ'. Inserting Eq. 3 into Eq. 4 and adjusting *K*' so that $A''(O'') = A''(0,0) = 1$ in the absence of the filter (i.e. $B'(\rho')$ = 1 and $\phi'(\rho')$ = 0) finally gives an integral expression of the complex amplitude distribution in the Lyot stop plane:

$$A''(\rho'',\theta'') = \frac{\pi R^2}{\lambda^2 F^2} \int_0^{+\infty} \int_0^{2\pi} \hat{B}_D(\rho') B'(\rho') \exp[i\phi'(\rho')] \exp[2i\pi\rho'\rho'' \cos(\theta''-\theta')/\lambda F] \, d\theta' \rho' d\rho' \cdot \tag{5}$$

Replacing $\hat{B}_D(\rho')$ with its analytical expression given in subsection 2.1 and introducing variable changes $u' = \rho'/\lambda F$ and $\beta = \theta' - \theta''$, relation 5 becomes:

$$A''(\rho'',\theta'') = \pi R^2 \int_0^{+\infty} J_1(2\pi R u') B'(u') \exp[i\phi'(u')] F(u'\rho'') \, du', \tag{6}$$

where:
$$F(u'\rho'') = \int_{-\theta''}^{-\theta''+2\pi} \exp[2i\pi u'\rho'' \cos\beta] d\beta = 2\pi J_0(2\pi u'\rho''), \tag{7}$$

and $J_0(z)$ is the type-J Bessel function at the zero order. Hence combining Eqs. 6-7 leads to:

$$A''(\rho'',\theta'') = 2\pi^2 R^2 \int_0^{+\infty} J_0(2\pi\rho'' u') J_1(2\pi R u') B'(u') \exp[i\phi'(u')] \, du' \cdot \tag{8}$$

Let us now study the simplest analytical case, where the circular grating is of the amplitude type with a cosine transmission function, i.e. $\phi'(u')$ = 0 and:

$$B'(u') = \frac{1+\cos(2\pi B u')}{2}, \tag{9}$$

with *B* the spatial frequency of the grating in the Fourier space. Then the spatial period of the filter in the image plane O'X'Y' is equal to $p' = \lambda F/B$ and its spatial frequency to $f' = B/\lambda F$. Eq. 8 can be expressed as:

$$A''(\rho'',\theta'') = \pi^2 R^2 \int_0^{+\infty} J_0(2\pi\rho'' u') J_1(2\pi R u') [1+\cos(2\pi B u')] \, du' \cdot \tag{10}$$

Omitting the multiplying factor $\pi^2 R^2$ in Eq. 10 to simplify the following analytical expressions, the complex aamplitude distribution diffracted by the image filter into the Lyot stop plane can be expressed as the sum of two different mathematical terms:

$$A''(\rho'') = A_0''(\rho'') + A_C''(\rho''),$$
$$\text{where:} \quad A_0''(\rho'') = \int_0^{+\infty} J_0(2\pi\rho'' u') J_1(2\pi R u') du' \tag{11}$$

and $$A_C''(\rho'') = \int_0^{+\infty} J_0(2\pi\rho'' u') J_1(2\pi R u') \exp(2i\pi B u')\, du' \cdot$$

Here the polar angle coordinate θ'' disappears since all functions are axis symmetric. Referring to mathematical textbooks [20-21], it is immediate that:

$$\begin{cases} A_0''(\rho'') = 1/2\pi R & \text{if} \quad \rho'' < R \\ A_0''(\rho'') = 1/4\pi R & \text{if} \quad \rho'' = R \\ A_0''(\rho'') = 0 & \text{if} \quad \rho'' > R \end{cases} \tag{12}$$

Finding an analytical expression for $A_C''(\rho'')$ makes use of reduced variables $r'' = \rho''/R$, $b'' = B/R$, and of a complex number representation writing as:

$$A_C''(r'') = \mathrm{Re}\left[\int_0^{+\infty} J_0(2\pi r'' u') J_1(2\pi u') \exp(2i\pi b'' u')\, du' \right], \tag{13}$$

with Re[z] denoting the real part of a complex number z. Next, inserting the integral representation of $J_1(2\pi u')$ that is:

$$J_1(2\pi u') = \frac{-i}{2\pi} \int_0^{2\pi} \exp\left[i\,(2\pi u' \cos\varphi + \varphi) \right] d\varphi, \tag{14}$$

Eq. 13 rewrites as:

$$A_C''(r'') = \mathrm{Re}\left[\frac{-i}{2\pi} \int_0^{2\pi} \exp[i\,\varphi] G(r'', \varphi)\, d\varphi \right]$$
$$\text{with:} \quad G(r'', \varphi) = \int_0^{+\infty} J_0(2\pi r'' u') \exp[2i\pi u'(b'' + \cos\varphi)] du' \cdot \tag{15}$$

The analytic expression of $G(r'', \varphi)$ derived from Refs. [20-21] is:

$$\begin{cases} G(r'', \varphi) = \dfrac{i}{\sqrt{(b'' + \cos\varphi)^2 - r''^2}} & \text{if} \quad r'' < b'' + \cos\varphi \quad (16a) \\ G(r'', \varphi) = \infty & \text{if} \quad r'' = b'' + \cos\varphi \quad (16b) \\ G(r'', \varphi) = \dfrac{1}{\sqrt{r''^2 - (b'' + \cos\varphi)^2}} & \text{if} \quad r'' > b'' + \cos\varphi\,. \quad (16c) \end{cases}$$

If $r'' \neq b'' + \cos\varphi$, the integration bounds of $G(r'', \varphi)$ are determined by the conditions $r'' < b'' + \cos\varphi$ and $r'' > b'' + \cos\varphi$, finally leading to an expression of $A_C''(r'')$ as:

$$A_C''(r'') = \frac{1}{2\pi} \int_{-\arccos(r''-b'')}^{+\arccos(r''-b'')} \frac{\sin\varphi\, d\varphi}{\sqrt{(b'' + \cos\varphi)^2 - r''^2}} + \frac{1}{2\pi} \int_{+\arccos(r''-b'')}^{2\pi-\arccos(r''-b'')} \frac{\cos\varphi\, d\varphi}{\sqrt{r''^2 - (b'' + \cos\varphi)^2}}\,, \tag{17}$$

where the first term vanishes since this is the sum of an odd function over opposite integration bounds. Now regrouping Eqs. 12 and 17, the final analytic expressions of the amplitude distribution $A''(r'')$ in the Lyot stop plane write as function of the reduced polar coordinate r'':

$$\begin{cases} A''(r'') = \dfrac{1}{2\pi}\left\{1 + \displaystyle\int_{+\arccos(r''-b'')}^{2\pi-\arccos(r''-b'')} \frac{\cos\varphi\, d\varphi}{\sqrt{r''^2 - (b''+\cos\varphi)^2}}\right\} & \text{if} \quad 0 \le r'' < 1 \quad (18a) \\ A''(r'') = \dfrac{1}{2\pi}\left\{\frac{1}{2} + \displaystyle\int_{+\arccos(1-b'')}^{2\pi-\arccos(1-b'')} \frac{\cos\varphi\, d\varphi}{\sqrt{1-(b''+\cos\varphi)^2}}\right\} & \text{if} \quad r'' = 1 \quad (18b) \\ A''(r'') = \dfrac{1}{2\pi} \displaystyle\int_{+\arccos(r''-b'')}^{2\pi-\arccos(r''-b'')} \frac{\cos\varphi\, d\varphi}{\sqrt{r''^2 - (b''+\cos\varphi)^2}} & \text{if} \quad r'' > 1. \quad (18c) \end{cases}$$

At first glance the previous expressions may involve elliptic integrals of the third kind [22] and the Heuman's Lambda function [23]. It turns our however that their modules and arguments should be complex, in which case no suitable analytical development can be found in the literature. Hence a numerical approach is preferred in the following sections.

2.3 Image/pupil stops inversion paradigm

Examining Eq. 18a in the special case when the reduced parameters *r''* and *b''* are equal to 0 and 1.respectively reveals that the complex amplitude $A''(0)$ is indeterminate mathematically, because the integration domain [+π,+π] reduces to zero, on the one hand, while the integrated function tends towed a negative complex infinite quantity $-i\infty$, on the other hand. This indeterminacy is at the heart of the present study and of the "inversion paradigm" for coronagraph circular gratings. Practically speaking, it corresponds to the case when the spatial frequency *f*' of the grating is equal to the cut-off spatial frequency of the telescope exit pupil, i.e.:

$$f' = B/\lambda F = R/\lambda F = 1/2\lambda N \tag{19}$$

with *N* the telescope aperture number. It follows that the spatial period of the grating is equal to $p' = \lambda F/B = 2\lambda F/D = 2\lambda N$, hence in most practical cases it is larger than one wavelength and typically equal to $2\lambda F/D$ for numerical simulations presented in the next section. Hence it should not be mistaken with sub-wavelength gratings employed in the vectorial vortex coronagraph [8].

Numerical simulations then show that $A''(r'')$ highly exceeds unity when *r*" tends toward zero. This is confirmed by the plots of Figure 4 showing it as function of *r''* (the red curve in the Figure), and the resulting intensity $I''(r'') = |A''(r'')|^2$ formed at the Lyot stop plane in logarithmic scale (blue curve in the Figure). Here the error bars represent the relative deviations between the results obtained by use of three different numerical models, being:

- Direct numerical integration of Bessel functions in Eq. 10,
- Numerical integration of analytical expressions in Eqs. 18,
- Fast Fourier transform (FFT) model of the diffracted intensity $I''(r'')$ as described in § 3.2.

It must be noticed that the amplitude of the error bars has been multiplied by a factor of 5 for better visualization of Figure 4. Discrepancies between the three models are actually lower than 0.1 % over 95 % of the range *r''* = [0 – 1.5] and always below 2 % on full range. One may thus conclude that the previous theoretical analysis is validated. More importantly, it shows that a high amount of the diffracted energy is located near the center O" of the Lyot stop plane when *b''* = 1, which will be the necessary condition for the inversion paradigm with respect to the historical Lyot design. Here the central occulting mask is no longer placed at point O' in the image plane O'X'Y', but moved to the O"X"Y" plane and centered at point O" as illustrated in Figure 2-B.

Finally, Figure 4 also evidences the presence of a faint halo surrounding the central peak in the O"X"Y" plane, which actually governs the final performance. The numerical simulations presented in the next section will be helpful to better characterizing this halo.

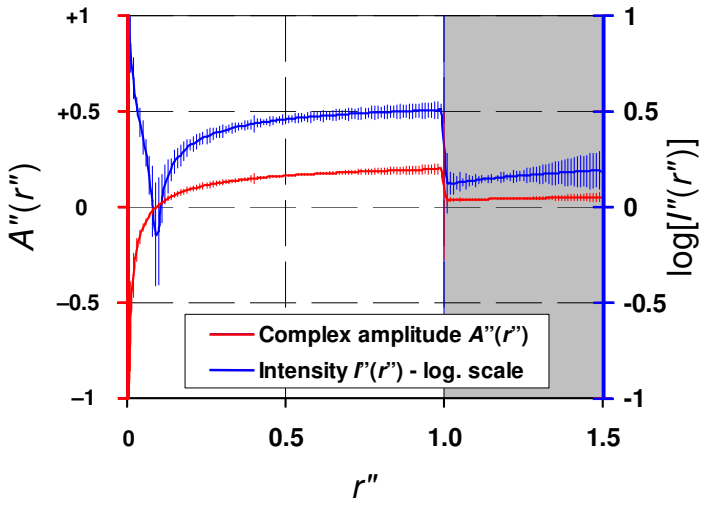

Figure 4: Plots of the complex amplitude $A''(r'')$ as function of r'' (red curve) and of the intensity $I''(r'')$ formed in the Lyot stop plane (blue curve in logarithmic scale).

3 NUMERICAL SIMULATIONS

Circular gratings commonly appear as a set of equally spaced, concentric circular slits [13-14]. However the panorama of circular amplitude or phase gratings is much more extended as will be seen in § 3.1. As such it requires using the numerical model described in § 3.2. Some preliminary and promising solutions are then presented in § 3.3.

3.1 Panorama of amplitude and phase gratings

There actually exists a wide variety of circular gratings: firstly, they can either be Circular amplitude gratings (CAG) whose diffracting pattern is coded into a gray scale transmission map varying between zero and unity, or transparent Circular phase gratings (CPG) introducing periodic phase distributions overall their surface. Ruled gratings or Volume phase holographic gratings (VPHG) belong to that second category. Next, the diffractive pattern can either be binary or continuous. In the latter case, various grating profiles may be designed, for example cosine or sine profiles, saw tooth profile and triangle profile. All of them can be "phase-shifted" by a quantity φ along the radial axis, whether they are binary or not. Binary CAG can be made of either equally-spaced black and white alternating strips, or of smaller or larger slit widths [12-13]. Continuous CAG functions can also be raised to the power of an integer or real number ξ with resulting grating transmission gains of losses. Finally, the axis symmetric geometry of CAG and CPG could be replaced with spiral geometry [12]. It follows that there exists a quasi-infinite number of solutions, especially when considering that the previous options can be combined with each other: for example saw tooth or triangle profiles can be phase-shifted or raised to the power of any number ξ, spiral gratings can be made binary, etc. Here six basic CAG options are defined analytically by the equations 20 in Table 1. They make use of the reduced radial coordinate $r' = \rho' B/\lambda F$ and are:

- Cosine: This the basic continuous profile already studied in § 2.2 including the additional phase-shift parameter φ (Eq. 20a),
- Saw tooth and Triangle continuous CAGs (Eqs. 20b and20c),

- Binary grating generated from the cosine formula 20a, equal to zero if it is lower than a certain threshold t_B and to unity otherwise (Eq. 20d),
- Power of ξ generated from the cosine formula 20a where the cosine term is raised to a power of ξ with $\xi > 0$ (Eq. 20e),
- Spiral, including an additional phase term equal to $s\theta'$ with θ' the polar angle and s the integer or real number of branches of the spiral (Eq. 20f).

Table 1: Six possible definitions of CAG profile functions.

Cosine	$B'_C(r') = 0.5 + 0.5\cos[2\pi(f'r' + \varphi)]$	(20a)
Saw tooth	$B'_{SW}(r') = [f'r'] \bmod 1$	(20b)
Triangle	$B'_T(r') = -2[\mathrm{sign}([f'r'] \bmod 1) - 0.5] \times [([f'r'] \bmod 1) - 0.5]$	(20c)
Binary	$B'_B(r') = 0$ if $B'_C(r') < t_B$ $B'_B(r') = 1$ otherwise	(20d)
Power of ξ	$B'_\xi(r') = 0.5 + 0.5\cos^\xi[2\pi f'r']$	(20e)
Spiral	$B'_{SP}(r', \theta') = 0.5 + 0.5\cos[2\pi f'r' + s\theta']$	(20f)

For what concerns CPG, their phase profile functions can easily be deduced from Eqs. 20 by use of the simple relation:

$$\phi'(r', \theta') = \phi'_0[2B'(r', \theta') - 1]; \tag{21}$$

with $\phi'(r', \theta')$ ranging in the interval $[-\phi'_0, \phi'_0]$, and ϕ'_0 is an additional design parameter defining the phase amplitude of the CPG. Graphical representations of the first five CAG functions are drawn in Figure 5 using the following parameters: $\varphi = 0$ and 0.25 in Eq. 20a, $t_B = 0.05$ in Eq. 20d, $\xi = 0.25$ in Eq. 20e. Arbitrary offsets and gain factors are applied for the sake of easier profiles visualization.

There is no doubt that analytical expressions similar to those of subsection 2.2 can be established, at the price of higher mathematical complexity. For CAGs they may involve decomposition in Fourier series as in Ref. [24], while the joint use of Jacobi's identities may be needed in the case of a CPG [17]. As interesting as they should be, such analytical developments are beyond the scope of the present study. This is the reason why a pure digital computing approach enabling numerical simulations of the previous CAG and CPG functions was preferred, and is described in the next subsection.

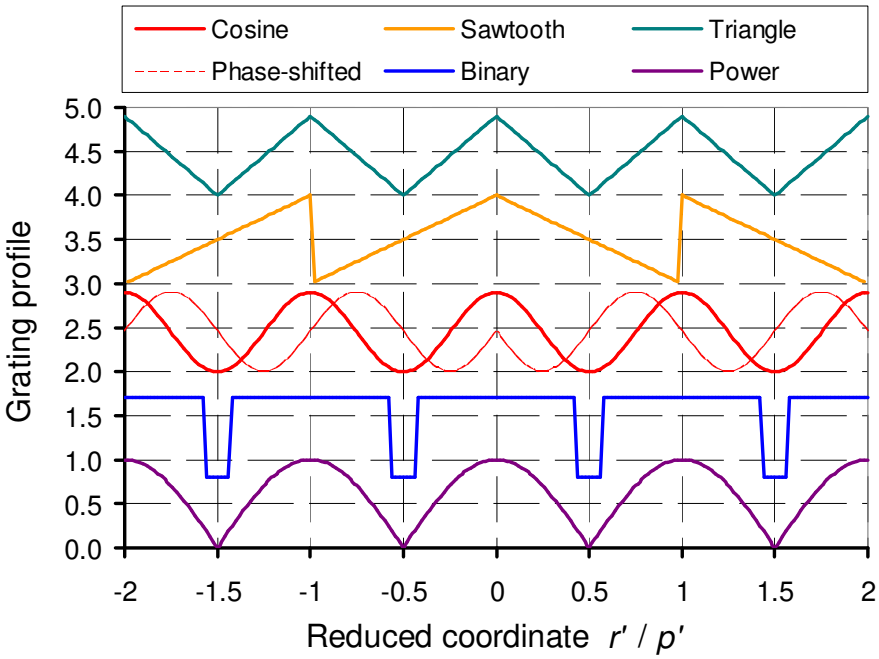

Figure 5: Illustrating various profiles of circular amplitude or phase gratings. Arbitrary offsets and gain factors are applied for the sake of easier profiles visualization.

3.2 Numerical model

The numerical model basically is a Fourier optics model propagating complex amplitudes throughout the optical system from the filter plane O'X'Y" to the final image plane of the coronagraph O"'X"'Y"' *via* Fast Fourier transforms (FFT). Only Fraunhofer diffraction is taken into account, Fresnel diffraction being neglected. The main steps of the computer code are the following:

1) Generate the complex amplitude in the filter plane O'X'Y" equal to $\hat{B}_D(\rho') = 2J_1(z)/z$ with $z = \pi D\rho'/\lambda F$ for an aberration-free telescope,

2) Multiply $\hat{B}_D(\rho')$ with one of the six generic CAG transmission function $B'(r',\theta')$ defined by Eqs. 20, or by the complex exponential $\exp[i\,\phi'(r',\theta')]$ if the grating is a CPG (see Eq. 21). The radius of the filter is always equal or higher than $10^3\ \lambda F/D$ in order to prevent aliasing effects,

3) Optionally, multiply $\hat{B}_D(\rho')$ with a mask function $M'(\rho') = B_{d'}(\rho') - B_{d'_{obs}}(\rho')$ with d' the maximal diameter of the filter and d'_{obs} the diameter of its central obscuration if any,

4) Compute the diffracted amplitude in the Lyot stop plane $A''(r'',\theta'')$ by taking the Fourier transform of $M'(\rho')B'(r',\theta')\hat{B}_D(\rho')$ or $M'(\rho')\exp[i\,\phi'(r',\theta')]\hat{B}_D(\rho')$ in the cases of a CAG or a CPG respectively,

5) Compute the intensity distribution in the Lyot stop plane $I''(r'',\theta'') = |A''(r'',\theta'')|^2$ and evaluate its maximal value I''_{Max}. Normalize $I''(r'',\theta'')$ so that I''_{Max} is equal to unity in the absence of the image filter,

6) Return to step 4 and multiply $A''(r'',\theta'')$ with a Lyot mask transmission function $M''(\rho'') = B''_{D_L}(\rho'') - B''_{D''_{obs}}(\rho')$ with D_L its maximal useful diameter and D''_{obs} the diameter of its central obscuration,

7) Compute the Fourier transform of the result to obtain the "nulled" complex amplitude distribution $A'''(\rho''',\theta''')$ in the final image plane of the coronagraph;

8) Take the square modulus of $A'''(\rho''',\theta''')$ to get the intensity distribution $N'''(\rho''',\theta''')$ in the image plane of the coronagraph. Evaluate its maximal value N'''_{Max} and normalize it so that it is equal to unity in the absence of the image filter and Lyot mask.

An illustrative example of the numerical model and of its main outputs is given in Figure 6 for the simplest CAG case that was analyzed in § 2.2. The different panels show a false color representation of the intensity distribution $I''(r'',\theta'')$ formed at the Lyot stop plane in logarithmic scale (a) and its surface plot (b), and similar plots for the intensity distribution $N'''(\rho''',\theta''')$ in the final coronagraph plane (c and d). The reader may also refer to Figure 4 showing radial plots of the complex amplitude $A''(r'',\theta'')$ and intensity $I''(r'',\theta'')$ at the Lyot stop plane. For a filter diameter d' = 0.01 mm (i.e. 10^3 $\lambda F/D$), that case leads to modest performance with a null ratio N'''_{Max} equal to 0.049 and a Lyot stop sized to D''_{obs}/D = 0.2 and D_L/D = 0.7. We also find that the maximal intensity peak is equal to I''_{Max} = 48.0 in linear scale. It is clearly visible at the centre O" of the Lyot stop plane in Figure 6-a. This result confirms the validity of the theoretical analysis. Moreover, it must be insisted on the fact that this basic case was introductory, and more promising solutions will be explored in the next subsection.

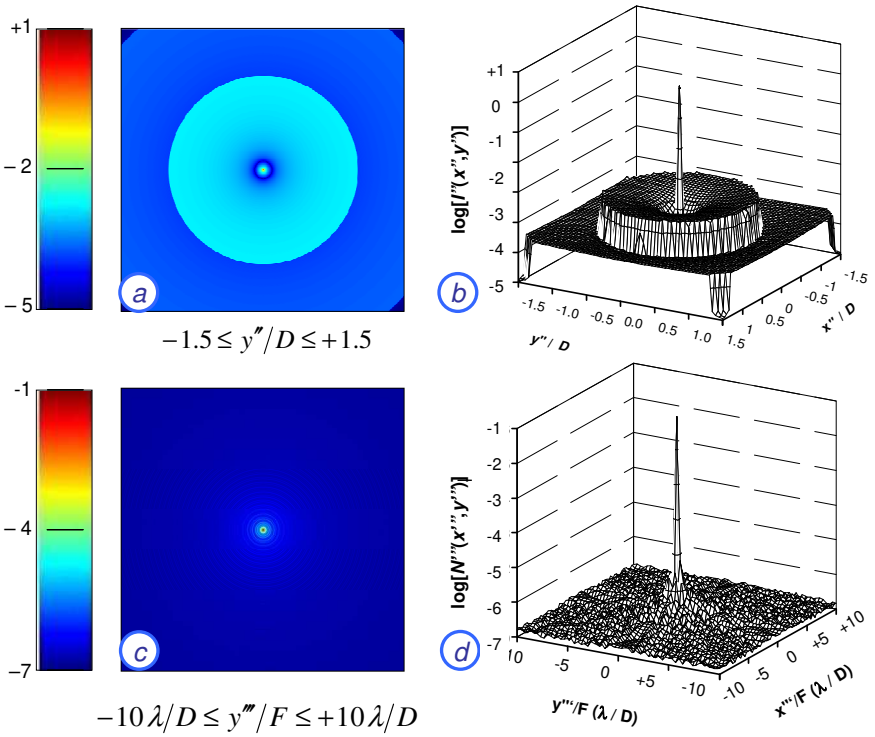

Figure 6: Plots illustrating the simplest CAG case defined in § 2.2. (a) False color representation of the intensity distribution $I''(r'',\theta'')$ at the Lyot stop plane (logarithmic scale). (b) Surface plot of $I''(r'',\theta'')$. (c) False color view of the intensity distribution $N'''(\rho''',\theta''')$ in the final coronagraph plane (logarithmic scale). (d) Surface plot of $N'''(\rho''',\theta''')$.

3.3 Preliminary solutions

Herein are presented the numerical results obtained for six preliminary circular grating designs of various types and parameters. They are summarized in Table 2, indicating the grating nature (CAG or CPG, binary or not), and its profile. The Table also specifies its amplitude ϕ_0' in the CPG case, its phase-shift if any, and the useful Lyot stop dimensions D_L and D_{obs}''. The two main performance metrics are the coronagraph transmission assumed to be fixed by the useful Lyot stop dimensions as $T = (D_{obs}''/D'')^2$ – note that for CAGs this definition does not include their intrinsic amplitude transmission function – and the central star null N_{Max}''' in the final coronagraph plane. The maximal irradiance I_{Max}'' on the Lyot stop plane is also given for information.
The six cases are illustrated graphically in Figure 7, showing grey-scale and false-color views of the grating for the CAG and CPG cases respectively, and surface plots and false-color views of the produced intensity distributions at the Lyot stop plane O"X"Y". They confirm the presence of the central peak intensity in that plane. It must be emphasized that this selection was not established at random, but results from a larger scale survey of different possible combinations of grating types and parameters. For example, it led to the following ascertainments:

- Continuous CAG profiles generally lead to modest performance in terms of star nulling ratio N_{Max}''', similar to the number obtained in the previous sub-section (~ 10^{-2}). Only a binary CAG profile may overcome that limit, but may suffer from transmission losses due to its nature.

- Conversely, better performance is attained by CPGs because their PTV amplitude ϕ_0' stands for an additional free parameter authorized to the designer,

- Whatever is the grating type and profile, no power of ξ different than $\xi = 1$ leads to improved performance,

- Spiral gratings are producing non axis-symmetric intensity distributions in the Lyot stop plane, suggesting that non symmetric Lyot stops may be preferred to symmetric ones (this option will be studied in the next section).

Finally, the reader might feel a bit disappointed by the relatively modest achieved performance, especially in terms of central star extinction N_{Max}''' that ranges here from 10^{-4} to 10^{-2}. Ways of improving the final performance of the optical system are described in the next section.

Table 2: Numerical results obtained for six preliminary circular grating designs of various types and parameters.

Case n°	Grating type	Is Binary ?	Grating profile	PTV amplitude (min/max)	Phase-shift (if any)	Lyot stop dimensions $D_{obs}'' - D_L$	Coronagraph transmission $T = (D_{obs}''/D_L)^2$	Maximal irradiance at Lyot stop I_{Max}''	Central star null N_{Max}'''
1	Amplitude	Yes ($t_B = 0.9$)	Cosine	0 / 1		0.2 – 0.7	0.45	34.4	6.0E-03
2	Amplitude	Yes ($t_B = 0.5$)	Sawtooth	0 / 1	π	0.2 – 0.7	0.45	103.0	7.1E-04
3	Phase	No	Cosine	± 2π		0.3 – 0.7	0.40	23.7	1.2E-03
4	Phase	Yes ($t_B = 0.5$)	Square	± π/2		0.3 – 0.7	0.40	401.2	1.4E-03
5	Phase	No	Triangle	± 4π		0.3 – 0.9	0.72	6.6	6.9E-05
6	Phase	No	Spiral, charge $s = 1$	± 5π/2		0.3 – 0.7	0.40	9.6	1.0E-02

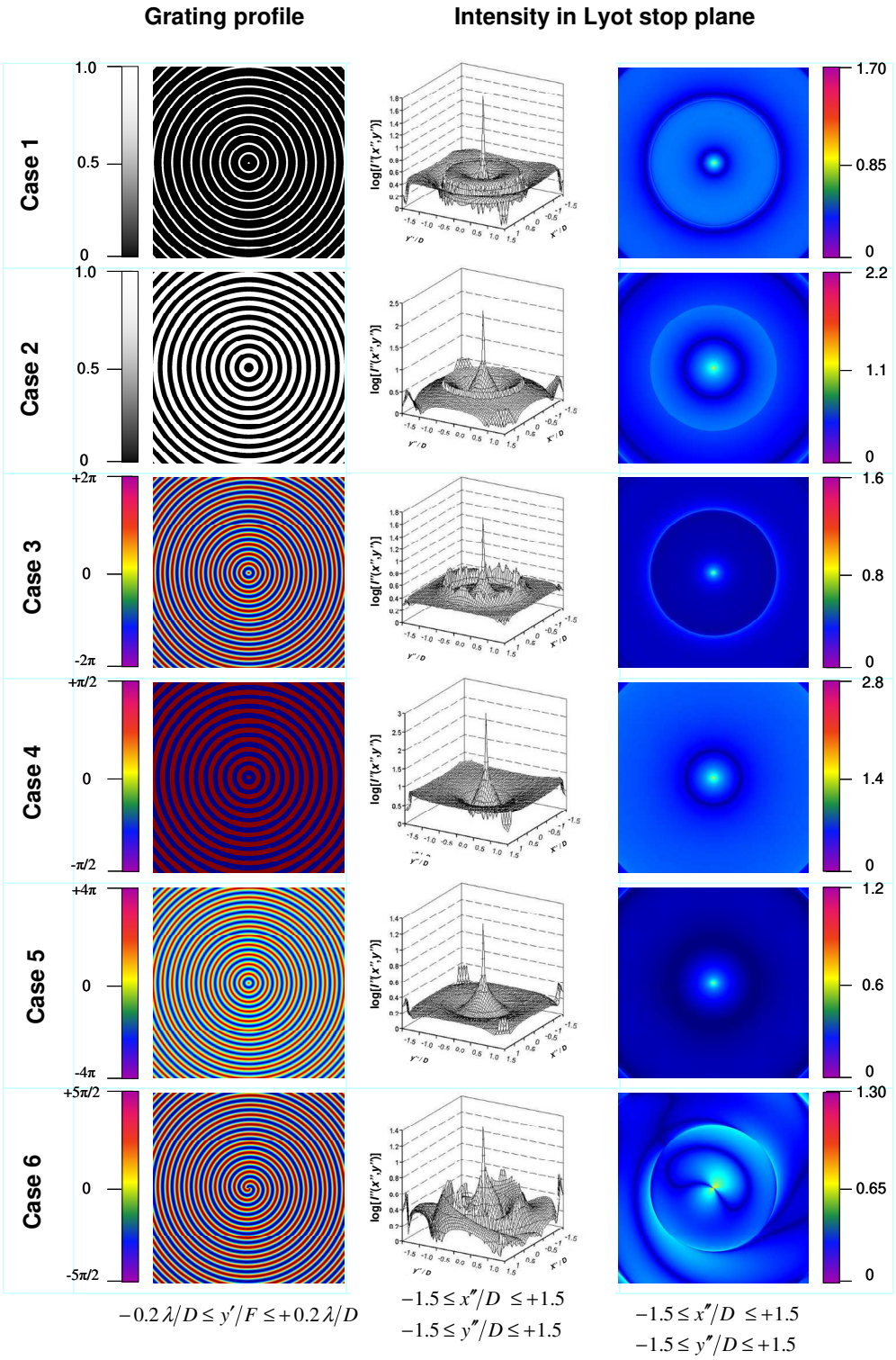

Figure 7: Plots illustrating the six cases defined in Table 2, showing grey-scale and false-color zooms at the central area of the grating (left column), surface plots of their produced intensity distributions at the Lyot stop plane in logarithmic scale (central column) and their representations in false-color (right column).

4 DISCUSSION AND ACHIEVABLE PERFORMANCE

Owing to the relatively modest performance attained by the six preliminary designs in § 3.3, this section firstly describes a more robust optimization procedure of the system and three examples of enhanced solutions (§ 4.1). Then subsections 4.3 and 4.2 describe the achievable performance of these designs in terms of planet transmission efficiency, and null ratio behavior over an extended spectral bandwidth.

4.1 Optimization procedure and enhanced solutions

The optimization procedure is based on the two following principles that are illustrated in Figure 8:

- Firstly, adding a central obscuration onto the filter mask function $M'(\rho') = B_{d'}(\rho') - B_{d'_{obs}}(\rho')$ used in subsection 3.2 , step n°3, in order to block the central lobe of the PSF in the O'X'Y' plane as for the historical Lyot coronagraph. This may be regarded as a slight departure from the inversion paradigm exposed in subsection 2.3, but practically leads to improving the null ratio N'''_{Max} by two orders of magnitude at least.

- Secondly, the Lyot stop mask should be adapted to the different grating shapes and parameters in order to further minimize the star nulling ratio, on the one hand, and to maximize the planet transmission efficiency, on the other hand. In particular, the light emitted by an extra-solar planet may be diffracted by the grating over a much larger area than the nominal circular Lyot stop of diameter D_L, (indicated by red circles. Hence the Lyot stop should be enlarged accordingly. Such over-sizing of the Lyot stop seems reasonable since most of the optical components inside a coronagraph module usually are of low numerical aperture, typically 0.05 or lower. On the other hand, the nulling ratio of the central star can be improved significantly by masking the brightest diffraction lobes observed in the Lyot stop plane O"X"Y". Thus the optimal Lyot stop should not remain circular, but instead be defined as:

$$\begin{aligned} M''(\rho'',\theta'') &= 1 \quad \text{if} \quad I''(\rho'',\theta'')/I''_{Max} < t_L \quad \text{and} \quad \rho'' < m_L D_L \\ M''(\rho'',\theta'') &= 0 \quad \text{if} \quad I''(\rho'',\theta'')/I''_{Max} > t_L \quad \text{or} \quad \rho'' > m_L D_L \,, \end{aligned} \tag{22}$$

where t_L is the Lyot stop threshold, and m_L its magnification factor.

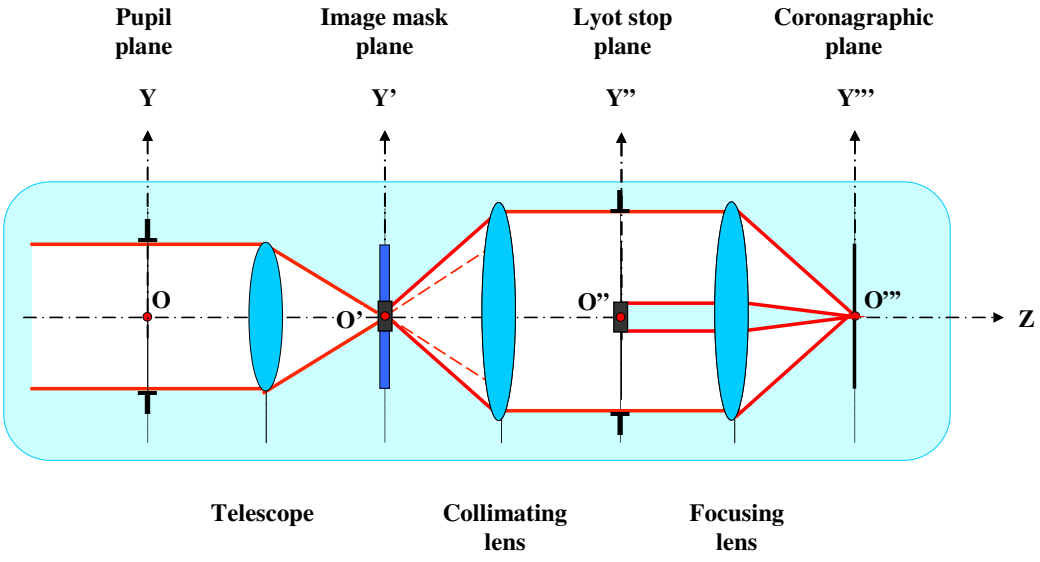

Figure 8: Sketch of the optimized CPG design illustrating the additional central blocking mask in the O'X'Y' filter plane and the enlarged Lyot stop in plane O"X"Y".

It finally turns out that the four main parameters to be optimized are t_L, m_L, the filter obscuration ratio d'_{obs} / d', and the phase amplitude ϕ'_0 of the CPG, since only this type of grating is considered below. The optimization process makes use of a Powell algorithm minimizing a cost function C defined as:

$$C = \sqrt{w_N N'''^2_{Max} + w_T \left(Min(T, T_{Min}) - T_{Min} \right)^2} \tag{23}$$

where $Min(u,v)$ denotes the minimal value of parameters u and v, T_{Min} is a target value for the minimal requested transmission (here chosen as 0.5) and (w_N, w_T) are weighting factors for the null rate and transmission respectively. The three optimized designs are built from the preliminary solutions named cases n° 3, 5 and 6 in Table 2, and denoted cases n° 7, 8, 9 and 9b in Table 3. The Table summarizes the major designs characteristics, including their shape and optimized parameters. It also gives an estimate of the coronagraph transmission (here assumed to be a simple ratio between the unmasked and maximal areas of the Lyot stop), and the nulling ratio N'''_{Max} achieved for the central star. These numbers are also illustrated in Figure 9-a to 9-d, showing black and white maps of the masks functions $M''(\rho'', \theta'')$ in the left column, false-color views of their transmitted intensities in logarithmic scale (central column), and false-color representations of the residual Nulling point-spread functions (NSF) in logarithmic scale on the rightmost column. One may note that the magnification factor m_L along the X"-axis differs from the Y"-axis, and the resulting dovetail patterns of the binary masks $M''(\rho'', \theta'')$ and of their transmitted intensities. This dissymmetry originates from the assumption that the extra-solar planet is located along the X'-axis only, which allows alleviating computing loads. Here there is no loss of generality, since in operation coronagraph instruments are usually rotated around the main optical axis in order to modulate planet signals.

The attained nulling rates are finally ranging from 1.6 10^{-7} (triangle, case 8) to 3.2 10^{-7} (spiral, case 9) and up to 7.8 10^{-7} (cosine, case 7). These numbers look satisfactory since they only characterize the instrumental design, and it is expected that they could be improved by one or two orders of magnitude by data post-processing. These numbers are compared with those achieved with a vortex coronagraph of topological charge 2 (case 10 in Table 3) that is often considered as one of the most efficient, with phase function writing as:

$$\phi'(\theta') = 2\theta' \quad , \tag{24}$$

The next steps of the numerical simulations consist in evaluating the actual transmission of an extra-solar planet located off the coronagraph axis, and the robustness of the central null over an extended spectral bandwidth. This is the scope of the two following subsections.

Table 3: Numerical results obtained for three enhanced CPG designs.

Case n°	Grating type	Grating profile	Phase amplitude ϕ'_0	Filter obscuration ratio ($\lambda F/D$)	Maximal irradiance at Lyot stop I''_{Max}	Lyot stop threshold t_L	Lyot stop magnification factor m_L (y" / x")	Coronagraph transmission estimate	Central star null N'''_{Max}
7	Phase	Cosine	± 2.92 π	12.4	125.4	6.4E-04	3 / 1.2	0.832	7.8E-07
8	Phase	Triangle	± 2.96π	8.0	13.1	9.6E-05	3 / 1.2	0.833	1.6E-07
9	Phase	Spiral, charge s = 3	± 1.99π	5.2	1.2	1.2E-04	3 / 1.2	0.836	3.2E-07
9b(*)	Phase	Spiral, charge s = 3	± 1.99π	5.3	1.2	9.9E05	3 / 1.2	0.747	4.2E-06
10	Phase	Vortex, charge 2	± 2π	0.	1.0	Not applicable	1 / 1	1.000	<1.E-07

(*) with telescope central obscuration = 0.2 D

4.2 Wavelength dependence

Also of uttermost importance are the variations of the nulling ratio at wavelengths λ' differing from the nominal one λ. Here again the numerical model was used to compute the nulling rates over an extended spectral bandwidth of 20%, i.e. $|(\lambda' - \lambda)/\lambda| < 0.1$. Plots of the results in logarithmic scale are shown in Figure 10 for the four considered cases. The highest sensitivity is found for the triangular shape CPG that is about two orders of magnitude. Conversely, the null ratio variations of the cosine and spiral-shaped CPG are less than one order of magnitude, which confirm that they are the best candidate designs. Such low wavelength sensitivity only involves the intrinsic properties of the grating, regardless of potential achromatization processes that could be introduced during the design and manufacturing phases, depending on the employed techniques. It gives a clear advantage to the CPG with respect to the vortex coronagraph, whose spectral bandwidth is much more limited as can be seen from the grey curve in Figure 10. This may be regarded as the most attractive feature of circular phase gratings employed as coronagraph image filters.

4.3 Dependence to planet field angle

A satisfactory coronagraph design should not only provide high attenuation factors (defined as the inverse of the star nulling ratio $1/N'''_{Max}$), but also good transmission to the off-axis extra-solar planet orbiting around the star. Since the transmission estimates given in Table 3 are only indicative, more accurate estimations of the planet transmission were carried out using the numerical model described in § 3.2. For this the complex amplitude in the filter plane $\hat{B}_D(\rho')$ computed at step 1 was simply decentred by a quantity equal to the planet field angle, and the remaining computation steps are unchanged. For the three selected designs, plots of their transmission curves in linear and logarithmic scale as function of a field angle varying from 0 to 100 λ/D are shown in Figure 11. They reveal moderate transmission performance, ranging from about 10% for the triangular shape (who exhibited the best nulling ratio) to 30% for the basic cosine-shaped CPG It is interesting to note that the transmission curve of the spiral-shaped CPG shows an oscillatory behavior between 10% and 40%, depending on the precise planet location. This probably makes it the best compromise between the nulling rate and transmission, provided that the planet location was previously determined by use of other techniques such as radial velocity or transit observations. Figure 12 also illustrates the intensity distributions produced by a planet located at 50 and 100 λ/D from the central star, showing that its image is well resolved over a limited number of pixels. The curves in Figure 11are also useful to define the Inner working angle (IWA) of the coronagraph, i.e. the angular separation for which the planet transmission is equal to half of its maximal value. They show a clear advantage of the vortex coronagraph achieving smaller IWAs, to be counterbalanced with its much narrower spectral bandwidth. Moreover, it may be noted that the IWA of a spiral CPG should be reduced by increasing the number *s* of its branches in Eq. 20f.

4.4 Effect of telescope central obscuration

Although this study is mainly focused on future spatial instruments, it is of interest to check if a CPG coronagraph could be implemented on ground telescopes with central obscuration. Such an obscuration of 20% radius has been introduced into the numerical model for the spiral case 9. The results are indicated in Table 3 (case 9b) and illustrated at the bottom row of Figure 9, showing the appearance of faint satellite rings around the central peak. It can be seen that the contrast is degraded by about one order of magnitude only (~ 4.10^{-6} vs. 3.10^{-7}), while no significant transmission loss occurs. Thus a CPG coronagraph looks well-suited to ground observatories.

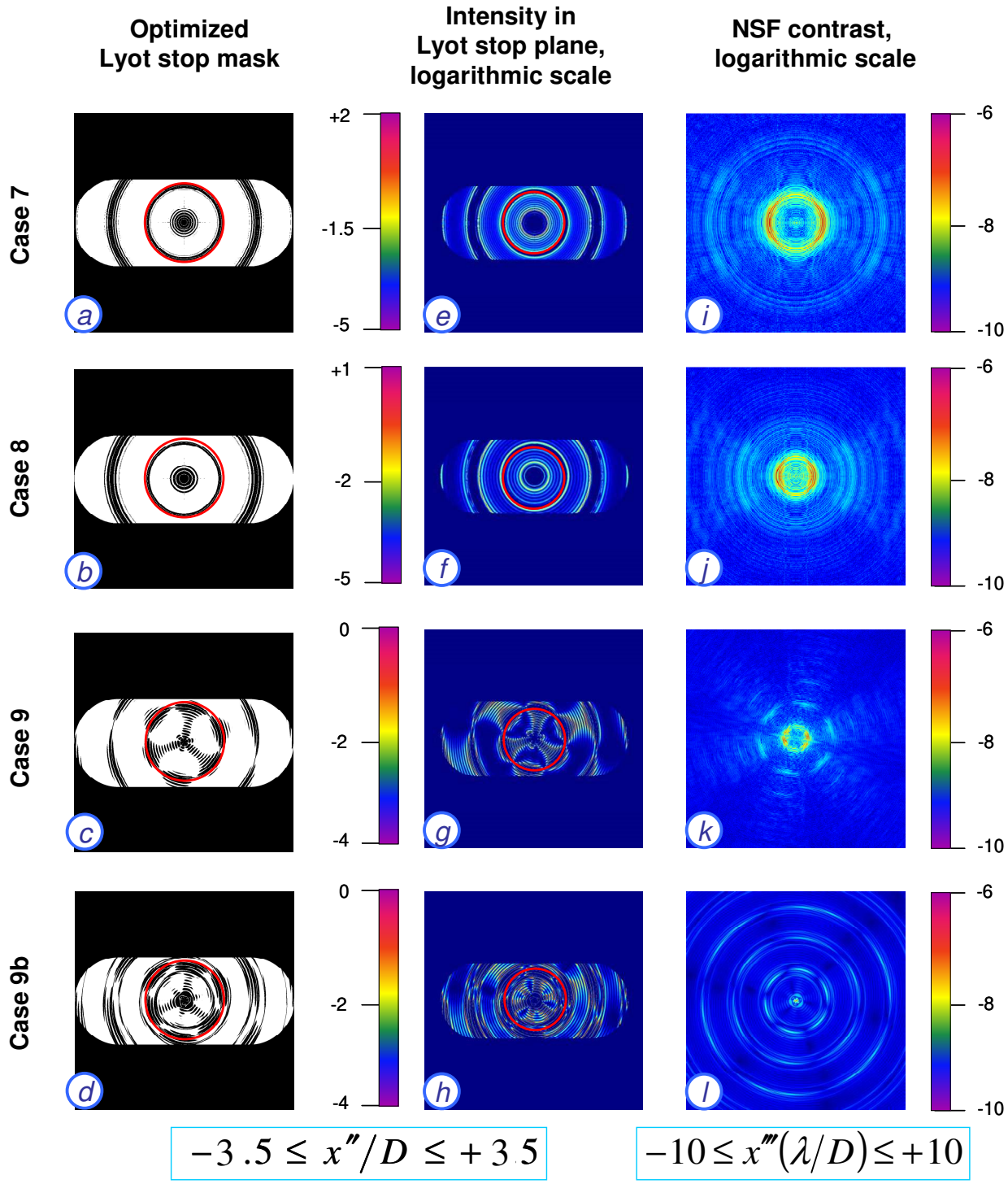

Figure 9: Optimized CPG solutions. From (a) to (d), the Figure shows black and white maps of the optimized Lyot mask $M''(\rho'', \theta'')$ for the cosine-shaped CPG (case 7), triangle-shaped CPG (case 8), and spiral-shaped CPG (cases 9 and 9b). From (e) to (h), false-color views of the transmitted intensities for these cases in logarithmic scale. From (i) to (l), false-color views of the resulting NSF in the O'''X'''Y''' plane in logarithmic scale. The diameter D_L of the initial circular Lyot stop is indicated by red circles. No central obscuration in the telescope pupil is present, except for case 9b where a central obscuration equal to $0.2D$ is introduced (d),(h),(l).

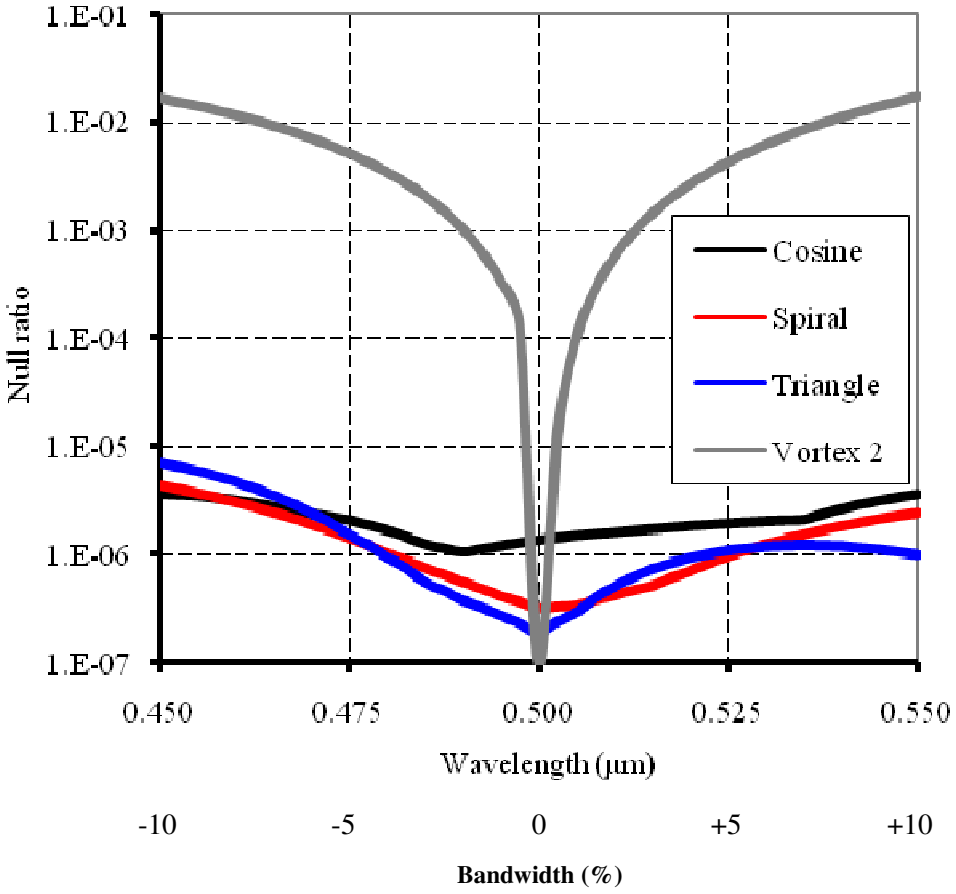

Figure 10: Plots of nulling rates in an extended spectral bandwidth (20%) for the three optimized designs 7, 8, 9 and the vortex coronagraph. The curves are shown in logarithmic scale.

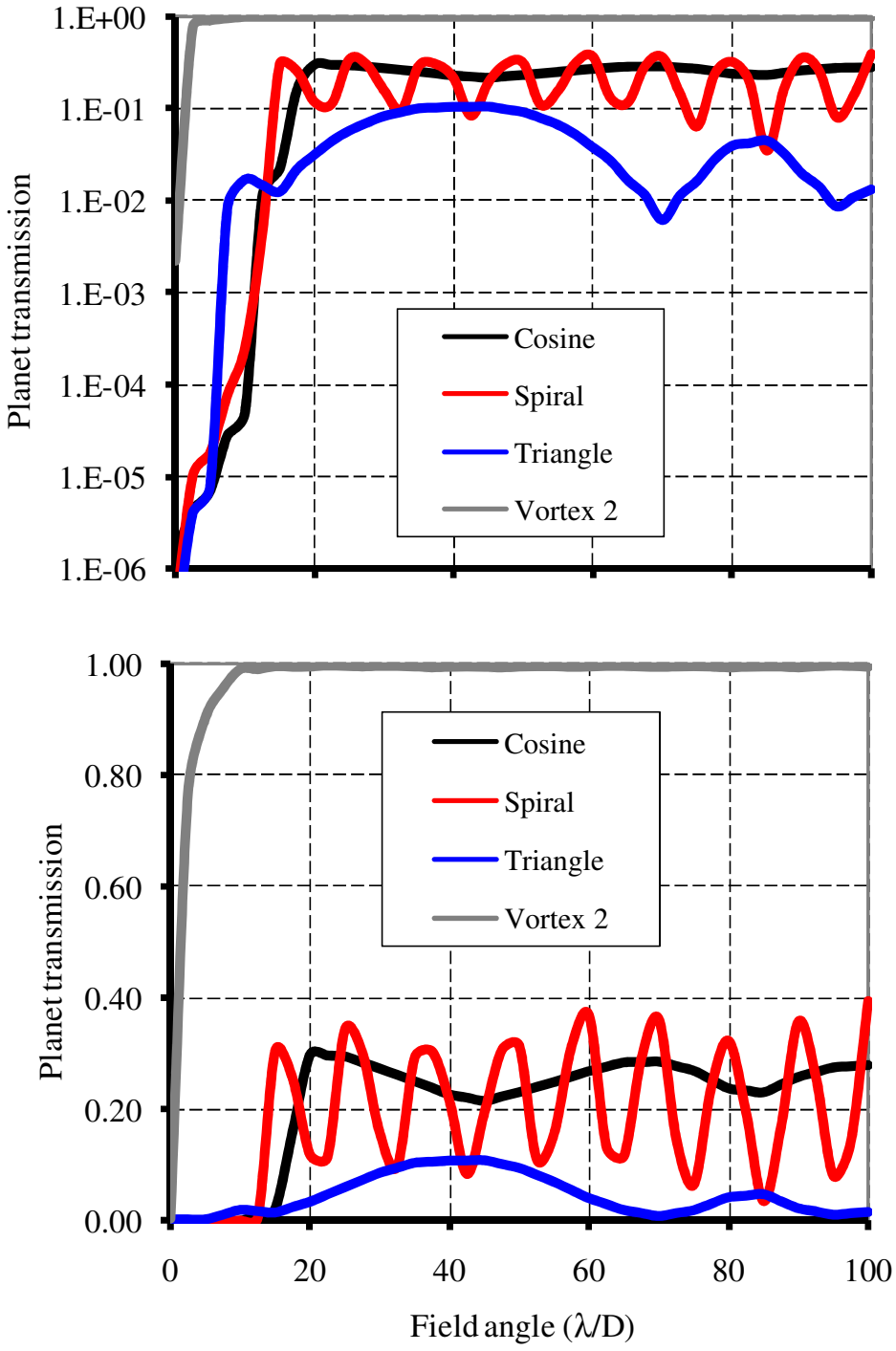

Figure 11: Planet transmission curves achieved by the three optimized designs (case 7 = cosine, case 8 = triangle, case 9 = spiral) compared with the vortex coronagraph. The curves are shown in logarithmic scale (top) and linear scale (bottom).

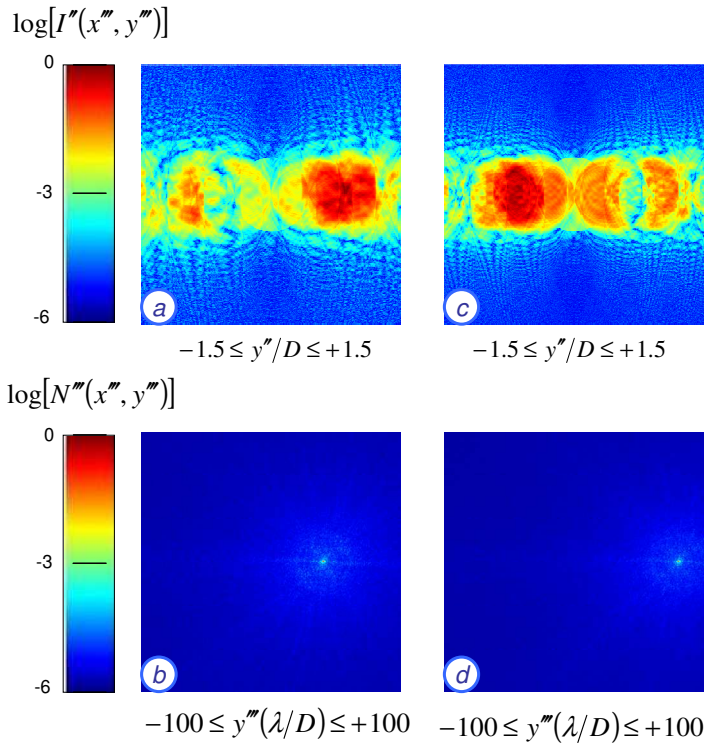

Figure 12: Illustrating the intensity distributions produced by an off-axis planet in the Lyot stop plane (top) and in the final coronagraph plane (bottom) for a target located at 50λ/*D* (a-b) and 100λ/*D* (c-d) from the optical axis. Plots are in logarithmic scale in order to enhance artifacts and residual speckles in the coronagraph plane.

5 CONCLUSION

Arriving at the end of this first journey through the realm of circular gratings applied to coronagraphy, it seems that we only scratched the external surface of a rich vein. However it is already possible to draw some conclusions. Firstly, when the spatial frequency of the grating is properly matched to the exit pupil of the system, such amplitude or phase gratings placed at an optically conjugated image plane of the instrument can generate a bright central spot at the Lyot stop plane. That point is undefined mathematically, but deemed to be equal to Infinity. This is at the origin of an inversion paradigm that consists in blocking the central area of the Lyot stop instead of the image plane as in the classical Lyot coronagraph. It is possible to find an analytical expression of the intensity distribution created at the Lyot stop plane for the simplest case, which is a circular amplitude grating with cosine profile, and revealing the existence of a faint halo surrounding the central peak. However, more complicated grating shapes exist, among which sawtooth, triangular, binary, spiral, or multiple combinations of them. Such a large number of cases can only be handled with a numerical model based on double Fourier transforms algorithm described in the paper.

Secondly, the numerical model has been coupled to an optimization procedure minimizing the extinction ratio of the central star and maximizing the transmission of extra-solar planets orbiting around it. Thus multiple grating shapes and their free design parameters can be explored. Moreover, it allows tailoring both the grating and Lyot stop transmitting masks to the global system design. This led to the conclusion that a spiral phase grating probably stands for the best compromise between star nulling ratio and planet transmission.

Thirdly; the GPG coronagraph has been compared with the vortex coronagraph that is considered as one of the most efficient nowadays. It turns out that the CPG exhibits worse performance in terms of transmission and inner working angle, on the one hand, but shows the unique ability to operating over a much larger spectral bandwidth, on the other hand. It can be concluded that both designs are very complementary.

Finally, it seems that these types of phase gratings could be employed for other applications than astronomy, such as laser beam shaping, particle trapping and manipulation, or biomedical optics. This capacity may be the scope of future work.

REFERENCES

[1] J.-L. Beuzit, M. Feldt, K. Dohlen, D. Mouillet *et al*, "SPHERE: a planet finder instrument for the VLT," Proceedings of the SPIE vol. 7014, n° 701418 (2008).

[2] B. Macintosh, J. Graham, D. Palmer *et a*l, "The Gemini Planet Imager," Proceedings of the SPIE vol. 6272, n° 62720L (2006).

[3] F. Zhao, "WFIRST-AFTA coronagraph instrument overview," Proceedings of the SPIE vol. 9143, n° 91430O (2014).

[4] B. Lyot, "The study of the solar corona and prominences without eclipses," Monthly Notices of the Royal Astronomical Society vol. 99, p. 580-594 (1939).

[5] F. Roddier, C. Roddier, "Stellar coronagraph with phase mask," Publications of the Astronomical Society of the Pacific vol. 109, p. 815-820 (1997).

[6] L. Abe, F. Vakili1, A. Boccaletti, "The achromatic phase knife coronagraph," Astronomy and Astrophysics vol. 374, p. 1161-1168 (2001).

[7] G. A. Swartzlander Jr, "Peering into darkness with a vortex spatial filter," Optics Letters vol. 26, p. 497-499 (2001).

[8] D. Mawet, P. Riaud, O. Absil, J. Surdej, "Annular groove phase mask coronagraph," Astrophysical Journal vol. 633, p. 1191-1200 (2005).

[9] A. Ferrari, R. Soummer, C. Aime, "An introduction to stellar coronagraphy," C. R. Phys. vol. 8, p. 277-287 (2007).

[10] O. Guyon, E. A. Pluzhnik, M. J. Kuchner, B. Collins, S. T. Ridgway, "Theoretical limits on extrasolar terrestrial planet detection with coronagraphs," Astrophysical Journal Supplement Series vol. 167 p. 81-99 (2006).

[11] F. Hénault, A. Carlotti, C. Vérinaud, "Analysis of nulling phase functions suitable to image plane coronagraphy," Proceedings of the SPIE vol. 9912, n° 99126K (2016).

[12] J. Dyson, "Circular and spiral diffraction gratings," Proc. R. Soc. Lond. A vol. 248, p. 93-106 (1958).

[13] D. Tichenor, R. N. Bracewell, "Fraunhofer diffraction of concentric annular slits," JOSA vol. 63, p. 1620-1622 (1973).

[14] A. Fedotowsky, K. Lehovec, "Far field diffraction patterns of circular gratings," Applied Optics vol. 13, p. 2638-2642 (1974).

[15] C. Zhou, J. Jia, L. Liu, "Circular Dammann grating," Optics Letters vol. 28, p. 2174-2176 (2003).

[16] S. Zhao, J. F. Wen, P. S. Chung, "Simple focal-length measurement technique with a circular Dammann grating," Applied Optics vol. 46, p. 44-49 (2007).

[17] F. Hénault, "Strehl ratio: a tool for optimizing optical nulls and singularities," JOSA A vol. 32, p. 1276-1287 (2015).

[18] M. M. Sanchez-Lopez, I. Moreno, J. A. Davis, B. K. Gutierrez, D. M. Cottrell, "Double-ring interference of binary diffractive axicons," OSA Continuum vol. 3, p. 1679-1690 (2020).

[19] M. Born, E. Wolf, *Principles of Optics* (Cambridge University, 1999).

[20] M. Abramowitz, I. A. Stegun, *Handbook of mathematical functions*, Dover Publications, INC., New York (1972).

[21] G. N. Watson, *A treatise on the theory of Bessel functions*, Cambridge University Press 2nd edition (1966).

[22] P. F. Byrd, M. D. Friedman, *Handbook of Elliptic Integrals for Engineers and Scientists*, Springer-Verlag Berlin Heidelberg New York (1971).

[23] Y. L. Luke, *Integrals of Bessel Functions*, Dover Publications (2014).

[24] F. Hénault, "Analysis of azimuthal phase mask coronagraphs," Optics Communications vol. 423, p. 186-199 (2018).